Chapter

Validating a CFD Simulation Approach by Ventilation Measurements for an Air-Cooled Salient Pole Model Generator

Bastian Diebel, Axel Walter-Krause,
Roland Jester-Zuerker and Babette Schwarz

Abstract

Pressure and flowrate measurements were conducted for an air-cooled salient pole hydro model generator in order to validate a computational fluid dynamics (CFD) simulation approach. The ventilation system of the model generator was driven by adjustable external fans, which allows detailed pressure measurements for a range of operating conditions. The CFD model to be validated consists of full generator geometry which is modelled in high geometrical detail. The steady-state multiple reference frame approach was chosen for the simulations, and the influence of different rotor-stator interfaces and turbulence models was investigated. The comparison of measurement and simulations includes the static pressure along the flow path through the machine, the performance map of the external fans, and an analytical approach to describe the dimensionless machine parameters of the model generator. Good overall agreement was found between measurement and CFD, which justifies the application of the presented simulation approach in the design of ventilation and cooling systems for hydro power generators. Qualitatively the CFD simulations reproduced all measured flow effects. Also quantitatively a good prediction of measured values was identified for a broad range of operating conditions. However, it was found that the simulation accuracy does not only depend on the numerical models in use but also on the specific operating conditions and their affiliated airflow characteristics.

Keywords: electrical machine, salient pole hydro power model generator, cooling and ventilation, computational fluid dynamics, rotor-stator interface, turbulence modelling, flow and pressure measurement

1. Introduction

Today's generator technology is highly efficient. Nevertheless, the remaining electromagnetic losses in the range of 1% of the generator's rated power produce a considerable amount of heat. To remove this heat from the machine, a safe and reliable ventilation and cooling system is designed during the layout process individually for each hydro power generator.

During commissioning of many hydro generators, the ventilation and cooling system is evaluated as a part of the efficiency measurement. In the case of detecting insufficient cooling performance at this stage of the project, changes of the ventilation design become expensive and time-consuming. Therefore, reliable tools for developing the cooling system early in the design phase are required. Within recent years, computational fluid dynamics (CFD) simulations became a commonly used tool for such applications. However, in order to achieve the required calculation accuracy, detailed validation of the simulations is mandatory.

Normally, during commissioning or operation of hydro power generators, the opportunities for detailed measurements are limited, especially due to unavoidable standstill for installation and removal of measurement equipment. To overcome this problem, Voith Hydro operates a fully functional salient pole model generator which allows detailed measurement campaigns for different machine configurations without the limiting boundary conditions that are found in operational hydro power plants. This includes but is not limited to the investigation of the ventilation and cooling system of the model machine.

For this model machine, the airflow of the ventilation and cooling system was investigated in detail. The static pressure was measured at 17 representative locations within the machine. Additionally, the flowrate was monitored for each of the two fans that are mounted on the top of the test rig in order to drive the ventilation circuit. To obtain the correct thermodynamic state of the cooling air, temperature, barometric pressure, and relative humidity were measured. Different rotational speeds of the electric machine as well as of the fans were investigated to evaluate the ventilation performance within a broad range of operating conditions.

In addition, CFD simulations using the commercial software Star-CCM+ were performed and compared to the measurements. The simulation model included the complete geometry of the model machine, with all relevant parts modelled in high geometrical detail. This allows a direct comparison with all available measurement locations. Instead of modelling the fans, the measured volume flowrate was specified for the respective operating point. The air-to-water cooler of the test rig was modelled as porous media. The steady-state multiple reference frame approach was used for all simulations. The influences of different modelling methodologies such as the choice of rotor-stator interfaces and turbulence models were investigated.

In the following, the measured machine configuration is described in detail. Afterward, the measurement setup and the simulation model are presented. Finally, the measurement data is evaluated, interpreted, and compared to the simulations. This includes the discussion of the static pressure along the flow path through the machine and the performance map of the fans. Also the machine pressure loss is evaluated by means of dimensionless parameters. For all presented data, the focus is on the comparison between CFD and measurement results.

2. Model generator configuration

As described in the previous section, measurement data for large hydro power generators is hard to obtain, as restrictions in accessibility and modifiability of operational machines do not allow extensive measurement campaigns.

To overcome this problem, Voith Hydro has developed a small-scale model generator that might be operated similar to representative machines for large hydro applications. The main objectives of this test rig are to obtain measurement data for the validation of design tools but also to develop and test new innovative products and product improvements for hydro power generators. Although a clear focus during the design of the test rig was on electromagnetic similarity, investigations in the field of generator cooling and ventilation are possible as well.

The following subsections give a short overview of the model machine and its investigated cooling and ventilation configuration.

2.1 Overview

The investigated model generator is a synchronous, salient pole electric machine as it is typical for hydro power applications. On the test rig, the shaft of the generator is connected to an electric motor that feeds mechanical power into the system. The electric side of the generator is connected to a frequency converter-driven grid simulator, which allows numerous operating conditions at rotational speeds up to 750 rpm and a maximum electric output of 1.1 MVA.

An overview picture of the model generator is shown in **Figure 1**. The machine is completely encapsulated and thermally insulated from the environment. The air cooling circuit is driven by two parallel radial fans that are mounted on the top of the test rig. One air-to-water cooler removes the heat from the system.

2.2 Ventilation design

As it is typical for salient pole hydro generators, the investigated model generator is fully air cooled. **Figure 2** shows a schematic of the ventilation design, with blue arrows indicating the flow path.

The airflow is driven through the machine by two adjustable radial fans mounted on the top of the test rig. On the pressure side of the fans, the air enters the machine on both sides in axial direction. From there on it splits into two different

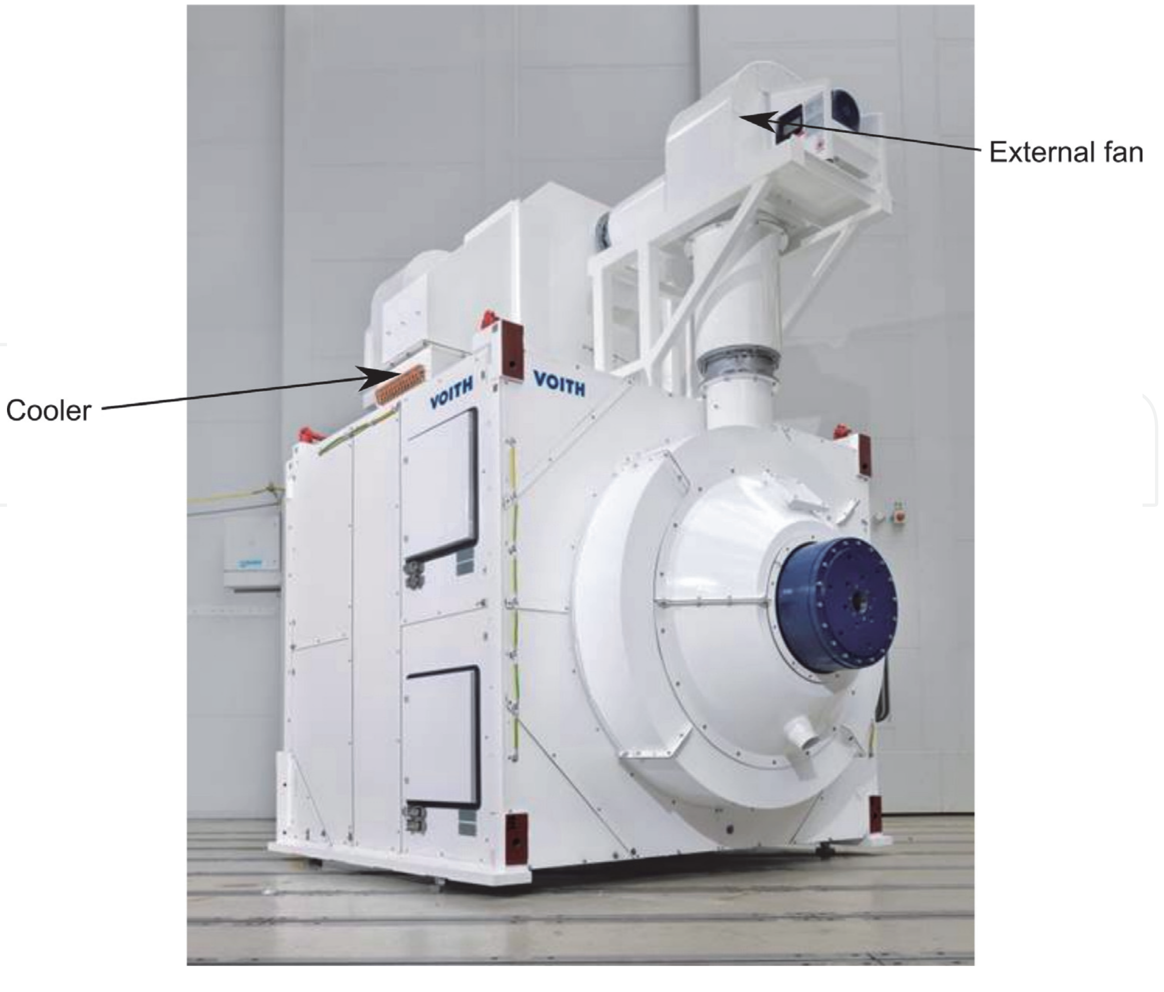

Figure 1.
Model generator overview.

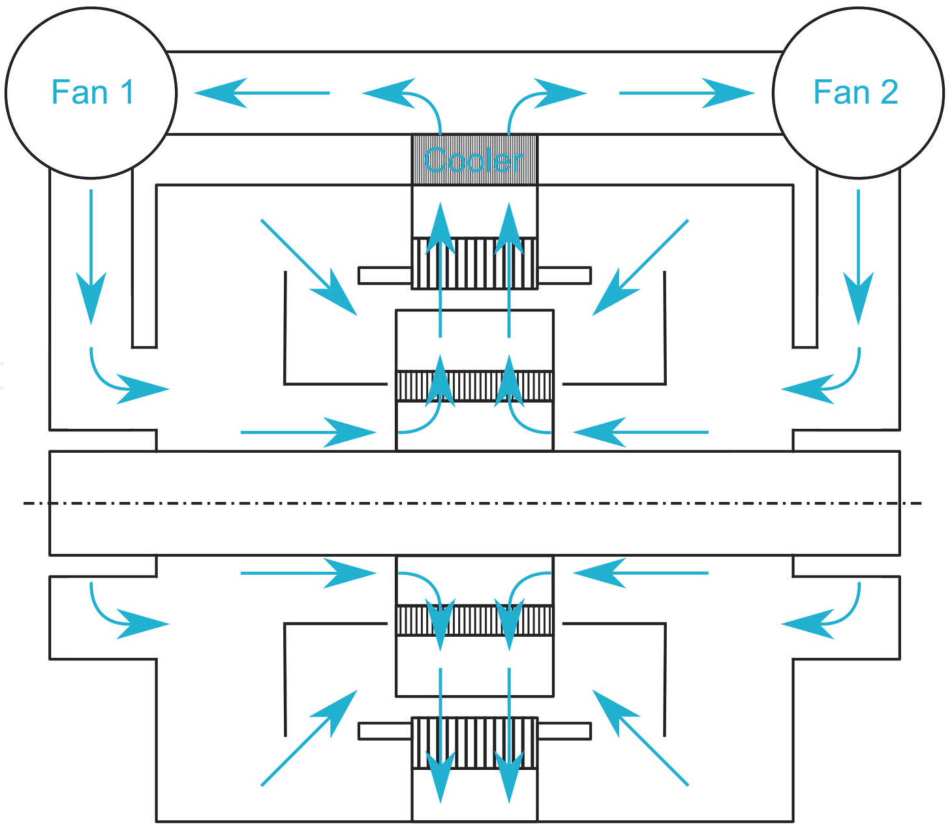

Figure 2.
Model generator ventilation scheme.

flow paths. The air on the first path directly enters the pole gaps and the annulus between rotor and stator (air gap) in axial direction. In the second path, the air enters the rotor hub openings close to the shaft in axial direction, from where it is guided radially outward into the pole gap via rectangular ducts. At this point, the two flow paths unite, and the air passes through the radial cooling ducts in the stator core toward the air-to-water cooler, where the heat is removed from the machine. After the cooler, the airflow separates into the two paths toward the fans, where the ventilation loop is closed.

Compared to the cooling scheme of most hydro generators in operation, two aspects are rather special about this model configuration: first, the split of flow paths in the rotor does not occur in most configurations as either all cooling air is guided radially through the rim or axially through the pole gaps. Second, most operating hydro generators have the air-to-water coolers distributed periodically around the stator circumference. For the given model machine, the cooler is positioned on the top of the test rig, which might lead to a less homogenous circumferential flow distribution in the stator core cooling ducts.

2.3 Operating conditions

As only the aerodynamic behavior of the investigated machine was of interest, all measurements were carried out without rotor winding excitation and in stator winding phase-to-phase short circuit.

To investigate a broad range of relevant operating conditions, measurement data was recorded for different rotational speeds of the electric machine, as well as for different rotational speeds of the two fans. Thereby, both fans were always run with the same rotational speed at a time.

Table 1 gives an overview of the investigated operating ranges. For each machine speed, measurements for four different fan speeds were done. In total,

Machine parameter		Investigated operating range
Rotational speed electric machine	$n_{Machine}$	0–750 rpm
Rotational speed fan	n_{Fan}	0–2932 rpm

Table 1.
Operating conditions overview.

measurements and CFD simulations for 12 operating points were conducted, which provides a full performance map of the model generator's ventilation system.

3. Measurement setup

The following sections shall provide a full overview of the measurement data that was obtained during the measurement campaign. Data was acquired for the static pressure at different positions of the machine, the thermodynamic state of the cooling air, and the volumetric flowrate through the model generator.

3.1 Static pressure

Static pressure was measured at 17 positions within the generator. All data was recorded relative to a common reference, which is the ambient pressure within the laboratory where the generator test rig is located. **Figure 3** indicates the pressure measurement positions within the machine. The pressure positions are named with abbreviations according to their location, which are documented in **Table 2**. The number behind the named positions indicates that multiple circumferential positions were measured, i.e., 1–2 indicates two circumferential positions, whereas 1–4 represents a circumferential distribution of four sensors.

All positions in **Figure 3** indicated with a dot represent single-spot measurements that were realized by locating an open end of a pressure tube at a position

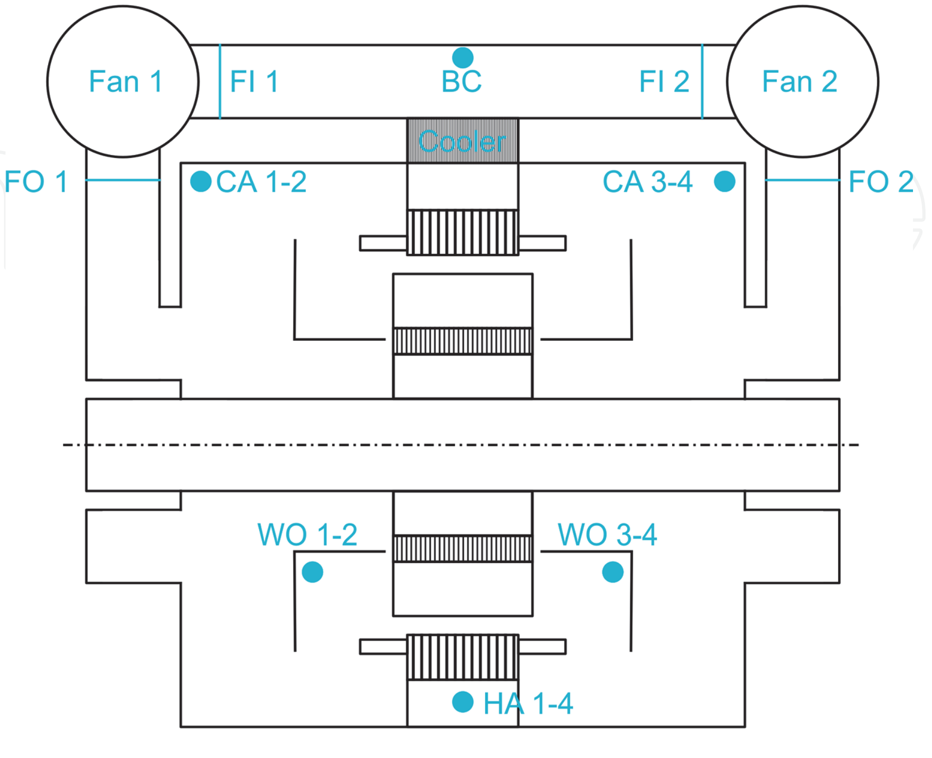

Figure 3.
Static pressure measurement positions.

where minimal flow velocities are expected (**Figure 4**). The positions indicated by a line (**Figure 3**, FI and FO) represent a wall pressure measurement at positions with higher flow velocities, i.e., before and after the fans. There, three wall pressure ports have been connected by a circular pipe to measure a circumferentially averaged wall pressure. An example for a circular pipe can be seen in **Figure 5**.

Abbreviation	Location
FI	Fan inlet
FO	Fan outlet
CA	Cold air compartment
WO	Winding overhang
HA	Hot air compartment
BC	Behind cooler

Table 2.
Abbreviations of measurement positions.

Figure 4.
Single-spot measurement.

Figure 5.
Circular pipe measurement.

All measurement data was acquired simultaneously by a multichannel pressure transducer. Data reduction was done for the recorded, time-resolved pressure data. Therefore, arithmetic averaging was done for each operating point after reaching steady-state operation. As pressure transducers tend to have a small zero drift, a correction of the recorded pressure readings was applied. To do so, the time-averaged data was subtracted by the time-averaged pressure reading at complete standstill of machine and fans. All static measurement data evaluation in this chapter is based on pressure data derived according to the procedure described above.

3.2 Thermodynamic state

The thermodynamic state of the cooling air was acquired by measuring the temperature T with a type A Pt100 temperature sensor and the relative humidity φ with a humidity sensor, both positioned on the cold air side of the machine behind the cooler. The absolute pressure p_a was measured in the laboratory. Using the data from the previously described static measurements, the absolute pressure in the closed air circuit behind the cooler was calculated using the formula:

$$p_{Cooler} = p_a + p_{BC}. \tag{1}$$

All data was time-averaged for each operating point, using an arithmetic average over all measured samples. With the described measurement data, the thermodynamic state of the cooling air within the model generator is well defined, and the cold air reference density was derived for each operating condition according to the ISO 5801 standard [1].

3.3 Volumetric flowrate

The flowrate of the cooling air was measured at the inlet of each of both fans. A Venturi type measurement principle was used, where the wall pressures for two positions with different cross-sectional areas at the fan inlet nozzle were measured and its pressure difference was correlated to the present flowrate.

The correlation of pressure difference and flowrate was done by an in situ calibration at the model generator. To do so, a calibrated measuring section was

Figure 6.
Volumetric flowrate calibration measurement section.

installed on the pressure side of each fan. The measurement section can be seen in **Figure 6**; it is connected to the fan via an air hose on the far end side in the picture. With this setup, calibration data was obtained for the full operating range of the fans in their actual assembly situation.

From the obtained calibration data, a formula was derived to directly correlate the pressure difference measurement at the fan inlets and the volumetric flowrate in the measurement section. In accordance with the theory for an incompressible, Venturi type flow meter [2], the flowrate $\dot{V}_{Fan}$ through each fan is defined by

$$\dot{V}_{Fan} = a \cdot \left(\Delta p_{Fan,Venturi} \cdot \frac{\rho_{ref}}{\rho_{Cooler}} \right)^{b}. \tag{2}$$

In this equation $\Delta p_{Fan,Venturi}$ is the relative pressure difference at the fan inlet nozzle, ρ_{ref} is the air density during in situ calibration, and ρ_{Cooler} is the density obtained for each measured operating point behind the air-to-water cooler (Section 3.2). Factors a and b are the calibration coefficients derived from the in situ calibration measurement data.

4. Simulation setup

In the following sections, the simulation model is described in detail. An overview is given for the modelled geometry and the computational domain. The numerical mesh is presented. Also, the applied numerical models are described, and an overview is given about the different investigated numerical setups.

4.1 Model overview

The simulation model included all relevant generator parts modelled in high geometrical detail. Due to the single cooler on the top of the test rig, no circumferentially periodic model segment could be derived as recommended in [3]. The CFD model featured the complete geometry of the machine. Though this led to high numerical effort, a direct comparison with all available measurement locations was possible.

Instead of modelling the fans, the measured volume flowrate was specified for the respective operating point. The cooler was modelled as porous media, where the pressure loss was taken into account by an additional momentum sink term in the equations being solved during the CFD simulation. The underlying porosity model (momentum sink) applies parameters which were derived from the pressure measurements.

An overview of the model is given in **Figure 7**. **Figure 8** shows a cut through the model, which allows a view on the rotor parts. Furthermore, the geometrically modelled perforated metal plates can be seen, which produce a uniform inflow into the cold air compartment. The walls of the parts form the boundaries for the fluid domains which were used for the CFD calculation. All in all there were three domains: one domain for the rotating parts, one for the stationary parts, and one for the porous cooler. All domains were connected by interfaces in order to form a coherent CFD simulation domain.

4.2 Meshing

A computational mesh was generated for each domain. The unstructured mesh consisted of polyhedral elements and two wall prism layers. The interfaces between

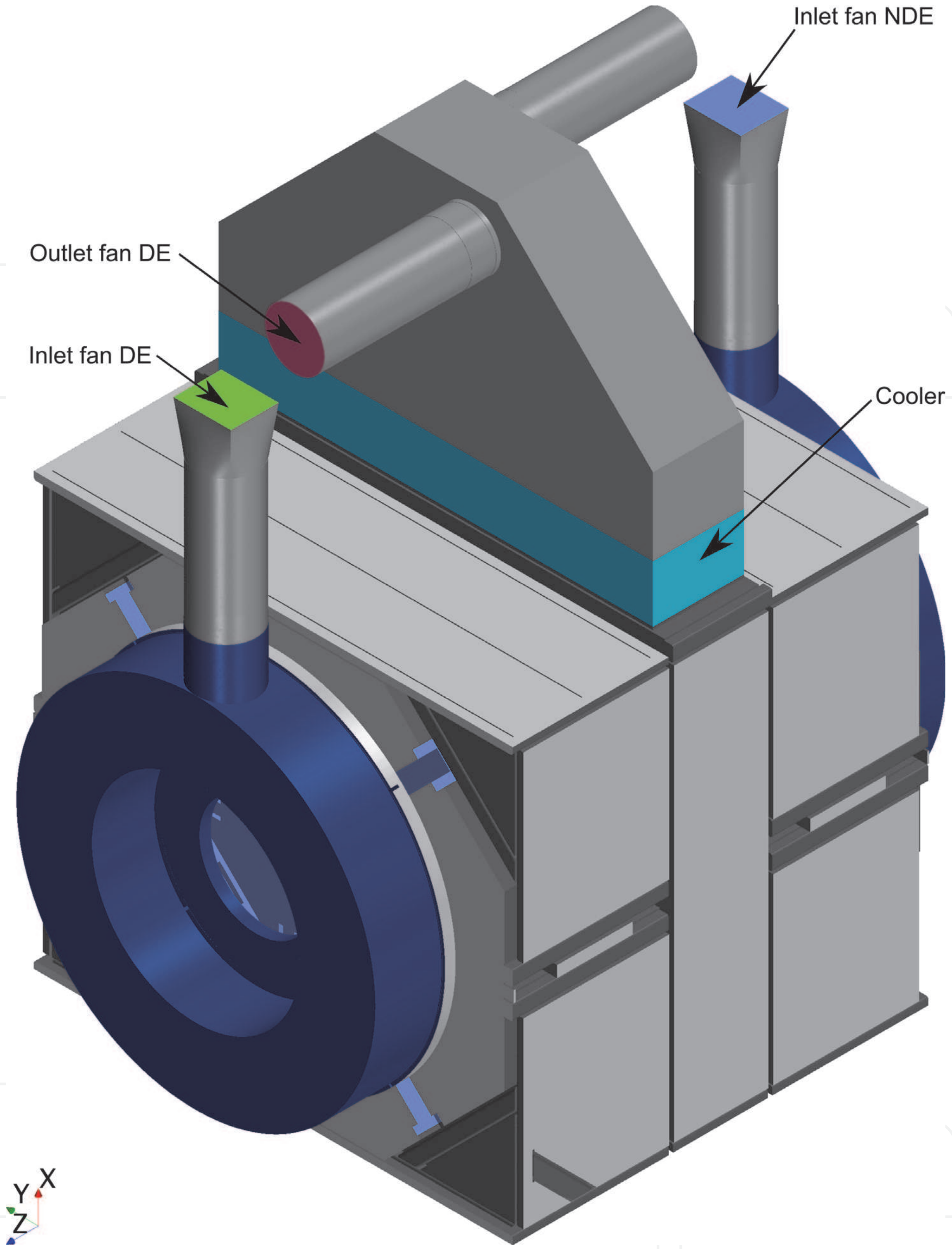

Figure 7.
Simulation model overview.

the domains were meshed node-conformal in order to improve the accuracy of the calculation. The total number of cells was 206.6 million.

In **Figure 9**, a section of the mesh within the pole gap can be seen. Inside the pole gap, the air cools the pole winding. To increase the heat transferring surface area, the pole winding is equipped with triangularly shaped cooling fins. To resolve this geometry feature, a fine mesh is mandatory.

Figure 10 shows the surface mesh of the rotor-stator interface, the cell size in the air gap between the interface and stator core, and one cooling channel. It can be seen that the mesh size is small in the area of the air gap and the intake of the cooling channels to resolve the high velocity gradients that are present in this area.

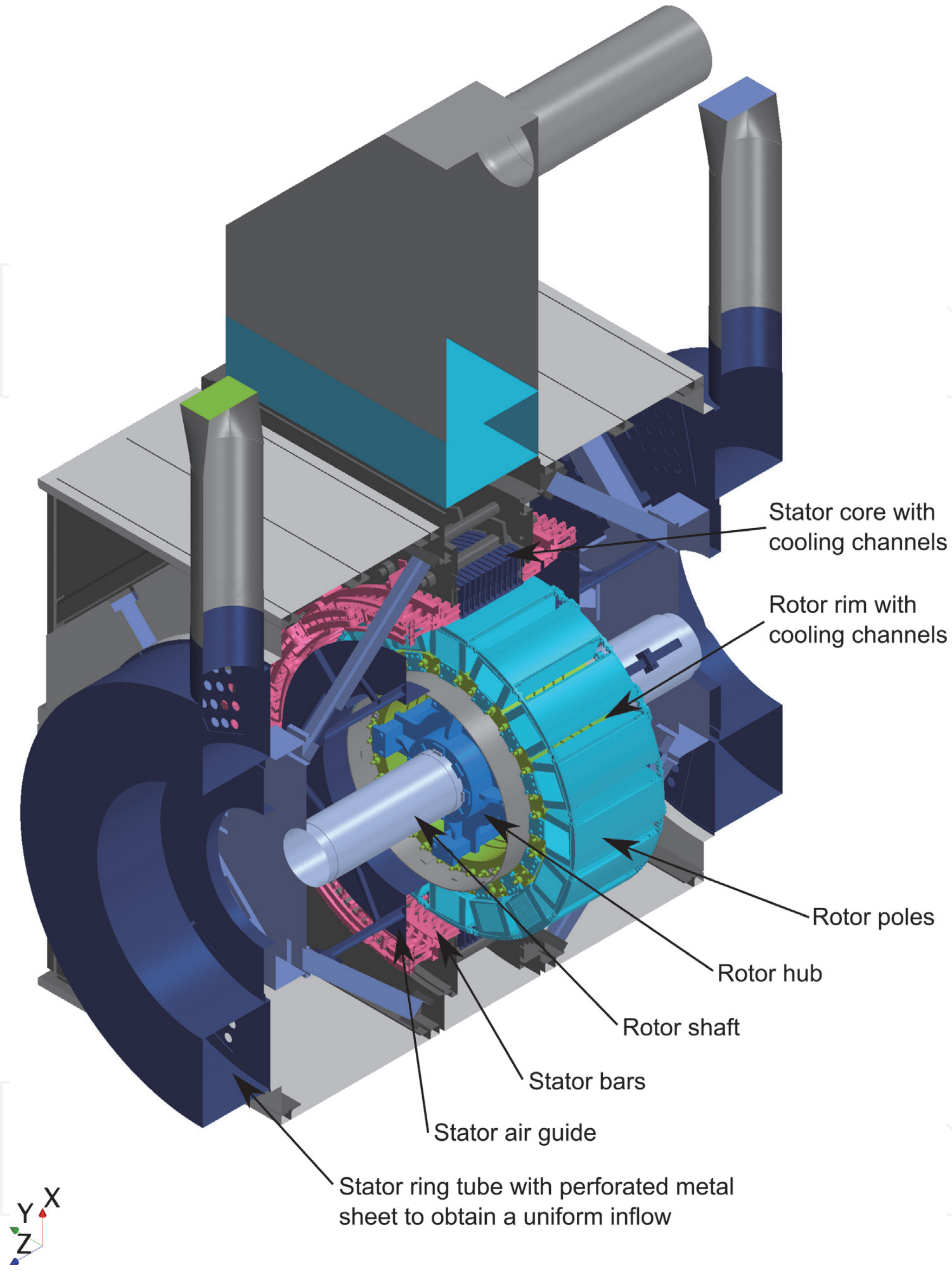

Figure 8.
Simulation model overview. Cut through stationary parts.

After entering the cooling channel, the airflow is guided in radial direction and is expected to develop a boundary layer similar to a turbulent channel flow with a low radial pressure gradient. This is why the cell size can be increased in radial direction in order to reduce the total number of cells.

4.3 Physical setup

An overview of the numerical setup is given in **Table 3**. All simulations were done using the segregated solver in the commercial software STAR-CCM+ v11.06. Steady-state RANS simulations [4] were conducted. The fluid was modelled with a

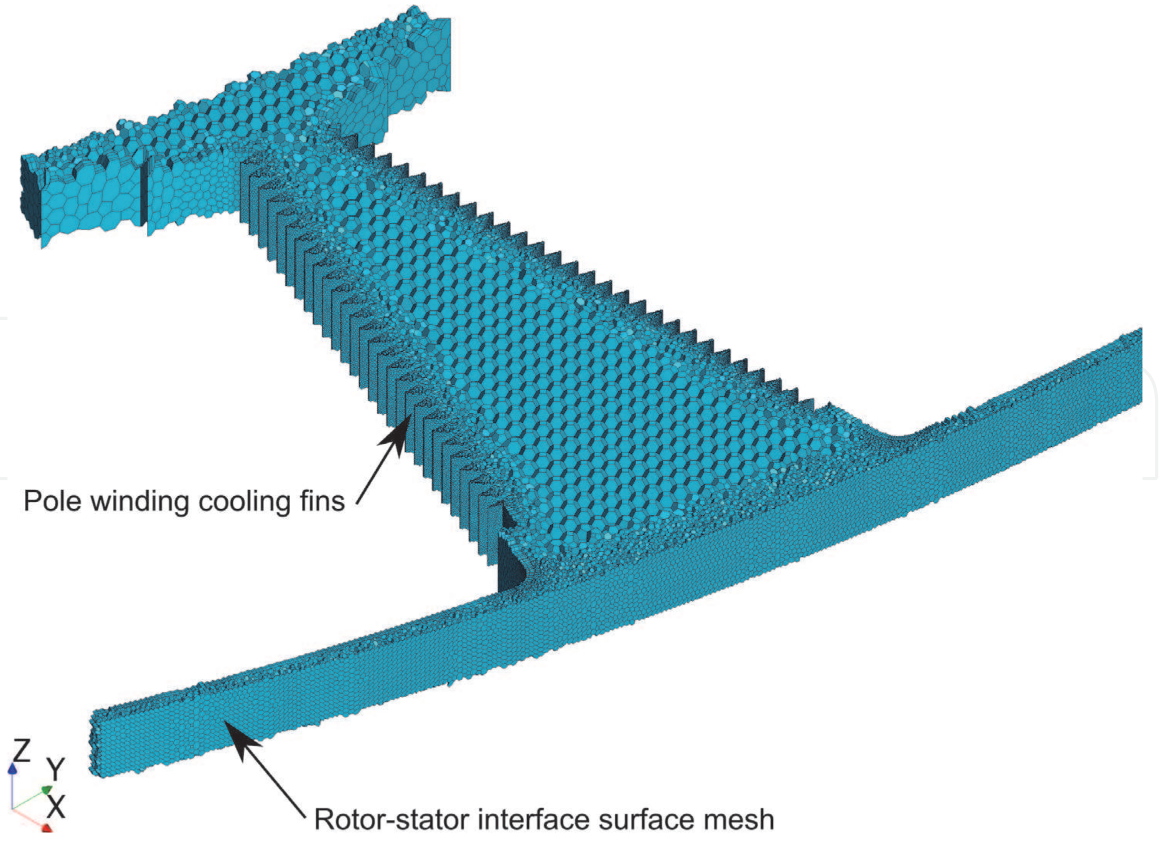

Figure 9.
Mesh overview. Pole gap.

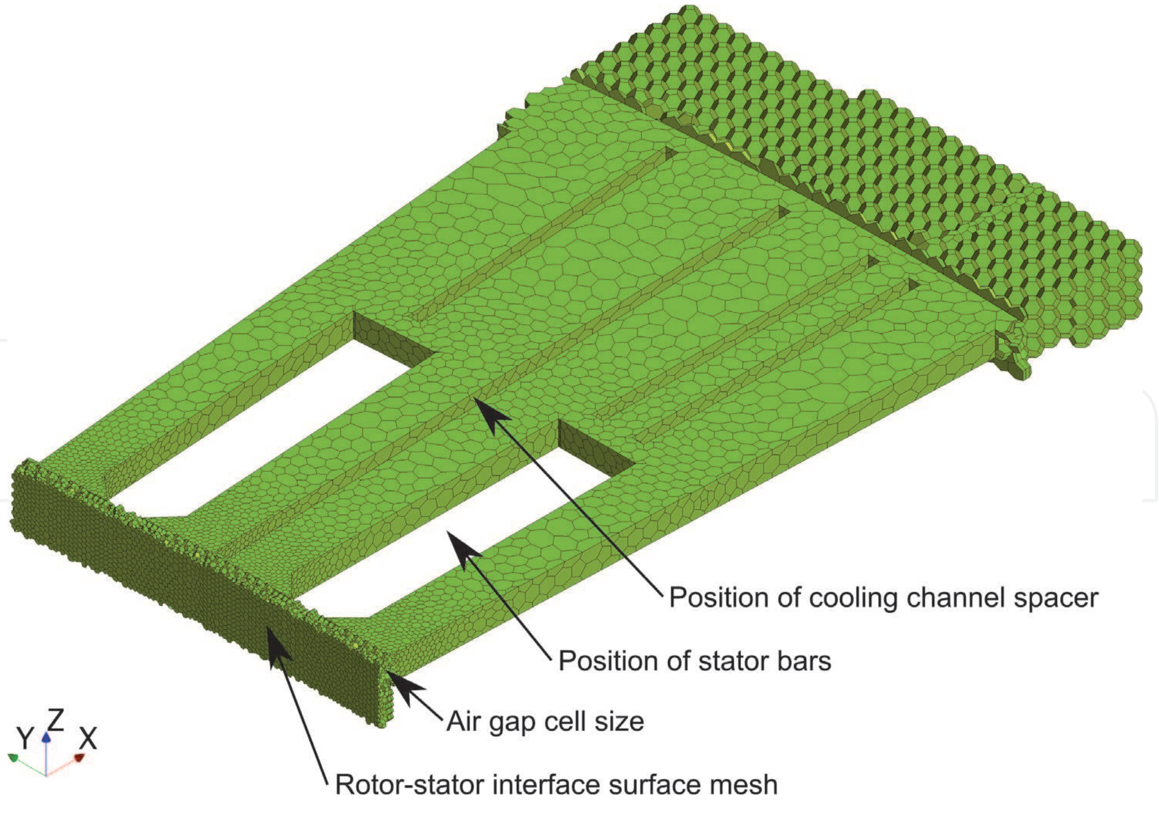

Figure 10.
Mesh overview. Stator cooling channels.

constant user-specified density and was considered isothermal. The density and dynamic viscosity were derived from the measured values (Section 3.2). The steady-state multiple reference frame approach was used for the simulation.

Solver	STAR-CCM+ v11.06
Analysis type	Steady-state
Rotor-stator interface	Frozen rotor/Mixing plane
Fluid model	Constant density
Heat transfer	Isothermal
Turbulence models	k-ε/k-ω SST

Table 3.
Physical setup overview.

Different modelling methodologies were investigated, including the influence of the frozen rotor and mixing plane rotor-stator interfaces and the effect of the k-ε [5] and k-ω SST [6] turbulence models.

Using the frozen rotor interface, the solution for one relative position of rotor and stator is calculated. The mixing plane interface leads to a circumferential averaging of the calculated flow quantities.

The k-ω SST turbulence model combines the benefits of the k-ε and k-ω turbulence model through blending. The k-ε turbulence model leads to better simulation results in free flows, whereas the k-ω turbulence model is expected to provide better turbulence modelling for near-wall flows [7].

5. Result evaluation

In the following sections, the CFD results are compared with the obtained measurement data. The pressure data for different positions in the machine is evaluated for a range of operating conditions. The focus of the evaluation is to identify coincidence as well as differences between the measurement data and the CFD simulation results with different numerical setups.

5.1 Flow path diagram

Figure 11 shows the averaged static pressure for each measurement position when following the flow path through the ventilation circuit. The values are normalized by the maximum fan outlet pressure that was measured for all operating conditions. The positions are named according to **Table 2**. For each flow path position, the value in the diagram is the average of all associated measurement positions that are available, e.g., CA 1–4 for the cold air compartment. The diagram shows the pressure plots for the four different fan speeds at a machine speed of 750 rpm. The other machine speeds have also been investigated but have shown qualitatively similar results, which is why only the 750 rpm variant is discussed here as representative example.

When the air passes through the fans, a static pressure rise can be observed for all operating points except for the point with fans turned off. In this case, consequently, a small pressure drop was measured. From fan outlet to cold air compartment, a pressure decrease can be observed, which is caused by a total pressure drop especially across the perforated plates mounted at the inlet of the cold air compartment.

In the cold air compartment, the static pressure of all operating points shown in the diagram approaches a value of zero. The reason for this is that in this area, there are several leaks to the outside of the machine, e.g., via the rotor shaft sealing. Therefore, the pressure equalizes with the ambient state in the laboratory.

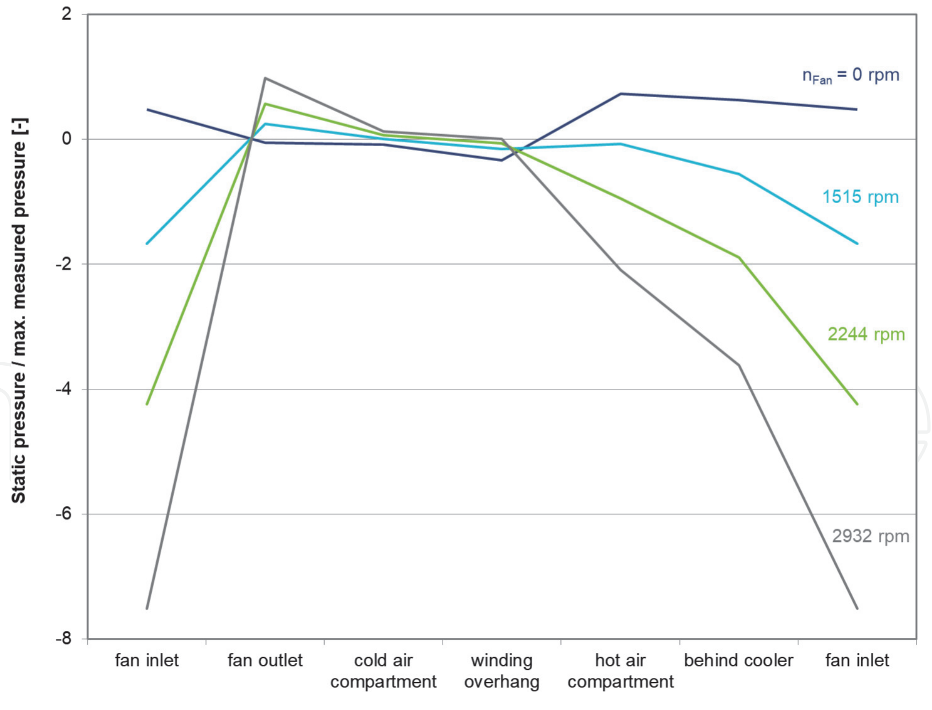

Figure 11.
Measured flow path diagram for $n_{Machine}$ = 750 rpm. Pressure values normalized by the maximum measured pressure.

Only a small pressure loss is observed from the cold air compartment to the winding overhang region for all operating points investigated. For the pressure drop from winding overhang to the hot air compartment, different effects can be seen, depending on the operating conditions.

With the fans turned off and at 1515 rpm fan speed, a pressure increase was measured. This is because the rotating components of the machine, comparable to a pump, transfer energy into the fluid which increases the total pressure of the system. In parallel, the flowrate provided by the external fans is rather low, leading to a low pressure loss within the ventilation circuit. Therefore, the pressure increase dominates over the pressure loss for the mentioned operating points. For the other operating conditions, the pressure loss in the machine is higher than its pressure buildup, as the external fans provide higher flowrates with increasing rotational fan speeds.

From the hot air compartment to the measurement position behind the cooler, a pressure drop can be observed for all operating conditions.

From the cooler outlet to the fan inlet, a comparably high pressure loss is present. This is due to the superposition of two effects: the total pressure loss along the flow path as well as a shift from static pressure to dynamic pressure as the cross-sectional area decreases when entering the duct toward the suction side of the fan.

The described pressure path is used to investigate the effect of different rotor-stator interface formulations and turbulence models. **Figure 12** shows all investigated combinations of rotor-stator interfaces (frozen rotor and mixing plane) and turbulence models (k-ε and k-ω SST) exemplary for the operating point with the highest machine and fan speed. The pressure level of the simulation data is adapted in order to obtain the same fan outlet pressure as in the measurements. The fan outlet is the inlet boundary of the CFD simulation model.

In **Figure 12** it can be seen that the calculated pressure drop between fan outlet and cold air compartment is approximately the same for all investigated combinations. Due to the fact that no rotor-stator interface is crossed, it can be stated that both turbulence models calculate the pressure drop for a combination of a duct flow

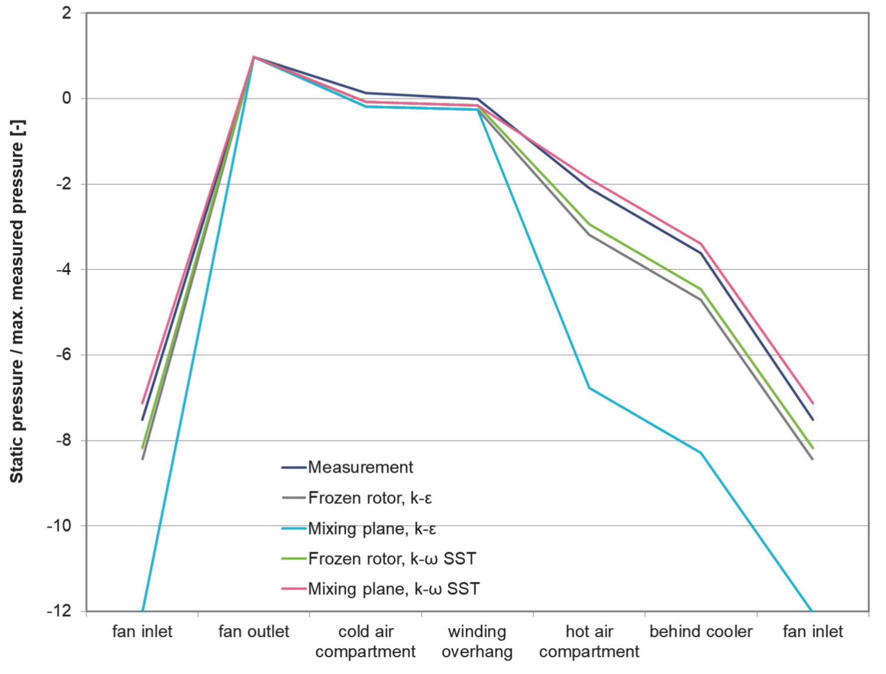

Figure 12.
Flow path diagram for $n_{Machine}$ = *750 rpm and* n_{Fan} = *2932 rpm. Pressure values normalized by the maximum measured pressure.*

and a geometrically modelled perforated plate in a stationary domain equally on the given mesh.

The major differences can be seen between winding overhang and hot air compartment. This is due to two effects. On the one hand, the influence of the rotor-stator interface can be observed, and on the other hand, the highest velocities and velocity gradients are present in this part of the machine. Therefore the influence of both, the rotor-stator interface and the turbulence model, can be seen.

For all simulations except for the combination of mixing plane interface and k-ε turbulence model, a comparable pressure drop is found. Both interfaces combined with the k-ε turbulence model calculate a rather high pressure drop. However, the combination of mixing plane and k-ε turbulence model overestimates the pressure drop significantly. Both interfaces in combination with the k-ω SST model lead to a good prediction of the pressure drop in this area, with the mixing plane model leading to the best agreement between measurement and CFD for the given operating point.

After the cooler, the pressure drop between cooler outlet and fan inlet is again comparable for all combinations.

Due to the high pressure drop for the combination of mixing plane interface and k-ε turbulence model between winding overhang and hot air compartment, the following evaluations were done for the k-ω SST model only.

5.2 Fan performance

The performance map of the ventilation circuit can be derived from the measurement data by plotting the pressure rise at the fans over the flowrate through the machine. As the static pressure before and after the fans was measured at positions with the same cross-sectional area and under the assumption that the velocity profiles in both positions are similar, it can be assumed that the static pressure rise is equal to the total pressure rise. **Figure 13** shows the performance map of the machine, with the static fan pressure rise Δp_{Fan} calculated according to **Table 2** as

$$\Delta p_{Fan} = \tfrac{1}{2}\left(\left(p_{FO\,1} - p_{FI\,1}\right) + \left(p_{FO\,2} - p_{FI\,2}\right)\right). \tag{3}$$

The differences in pressure rise and flowrates between both fans are small which justifies the averaging that is done in Eq. (3). The values in **Figure 13** are normalized by the maximum measured value for each fan pressure rise and volumetric flowrate.

The colored lines of constant machine rotational speed can be interpreted as consumer characteristic of the test rig, and the gray lines of constant fan rotational speed characterize the provider side of the setup.

With the fans turned off, a positive flowrate can be observed for machine speeds of 375 and 750 rpm. This is due to the rotating parts of the machine (pole, rim, hub) working on the fluid. The corresponding operating range is called self-ventilation.

When increasing the fan speed, the influence of self-ventilation is reduced, and the pressure rise due to the fan becomes the dominating flowrate source in the ventilation circuit. Therefore, the performance map shrinks to a rather narrow band, especially with comparably small differences between the consumer lines for 0 and 375 rpm. For the present machine setup, the maximum flowrate is reached at 750 rpm machine speed and 2932 rpm fan speed.

In **Figure 14** the performance map calculated from CFD with frozen rotor interface is shown. **Figure 15** shows the results for the mixing plane interface. Again, both diagrams are normalized by the maximum pressure and flowrate obtained from the measurements. To allow a direct comparison, the measured performance map is indicated by dashed gray lines.

In general it can be stated that the results for both interface models qualitatively agree well with the measurement data. All effects described above are represented in the simulation results, including the negative pressure rise in the area of low flowrates and the narrowing of the consumer lines at higher flows.

When concentrating on the machine speeds 0 and 375 rpm, also good quantitative agreement is reached between simulations and measurement for both interface formulations. The mixing plane results match the measured performance map well,

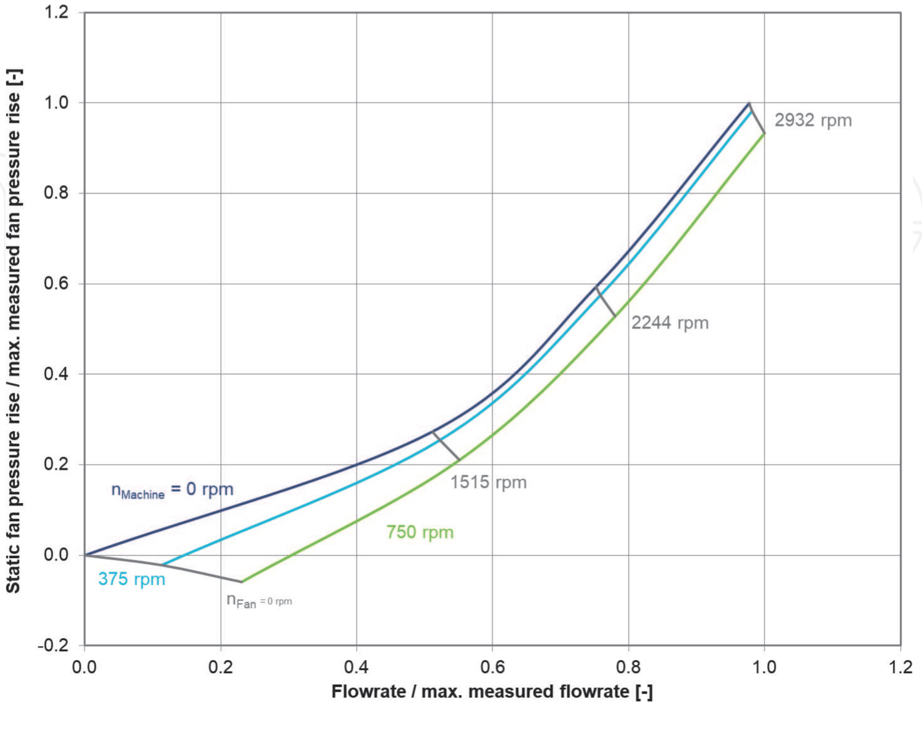

Figure 13.
Measured fan performance map. Values normalized by the maximum measured fan pressure rise and the maximum measured flowrate.

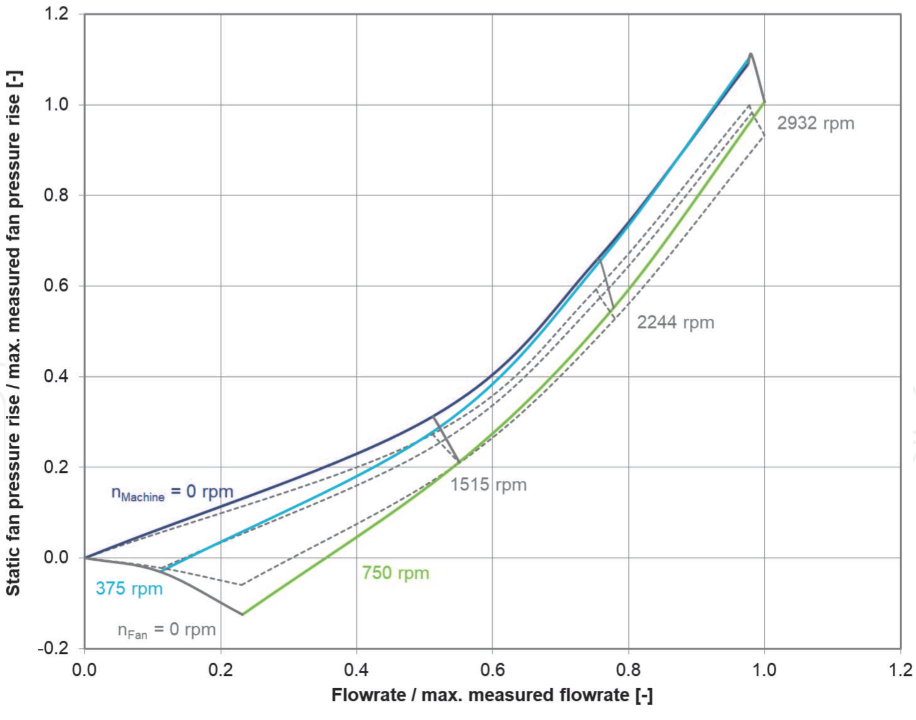

Figure 14.
Fan performance map calculated from CFD with frozen rotor interface. Thin dashed lines indicate the measured performance map for comparison. Values normalized by the maximum measured fan pressure rise and the maximum measured flowrate.

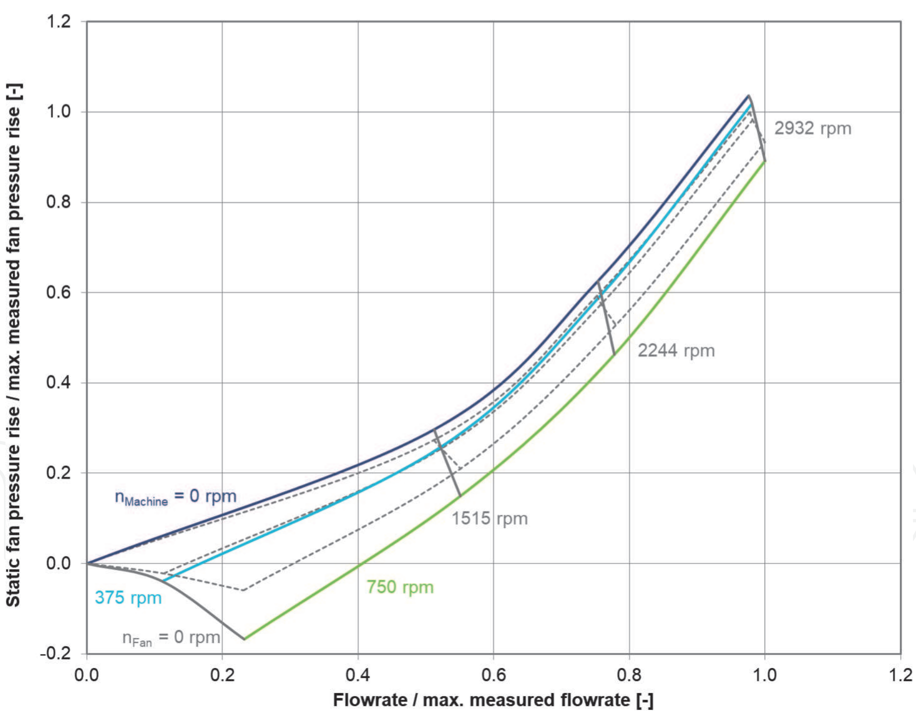

Figure 15.
Fan performance map calculated from CFD with mixing plane interface. Thin dashed lines indicate the measured performance map for comparison. Values normalized by the maximum measured fan pressure rise and the maximum measured flowrate.

especially in the area of higher flowrates. In this area, the frozen rotor interface tends to overestimate the machine's pressure loss.

Rather significant differences can be found at 750 rpm machine speed, particularly in the self-ventilation area with low flowrates. In this operating range, both interface models overestimate the negative pressure rise that is provided by the rotating electrical machine itself. This can be seen especially for the mixing plane interface where the negative pressure rise in the case of the fans turned off is predicted roughly two times higher than measured. This is an important finding as it shows that the simulation model reveals some sensitivity in predicting absolute pressure values when rotational effects dominate over the pressure loss of stationary parts in the system.

To evaluate the different predictions of such rotational effects, a closer look at the simulation results for 750 rpm machine speed and fans turned off shall be taken in the following. **Figure 16** shows static pressure plots for both interface definitions through the axial center of the machine. The pressure values are normalized by the magnitude of the measured fan pressure rise at the investigated operating point. The rotor pole gap, the air gap where the rotor-stator interface is positioned, and the stator core ventilation ducts can be seen in the picture.

First of all it can be noted that both contour plots appear very similar, with a qualitatively comparable pressure distribution. For both simulations, the absolute pressure difference depicted in the plot is higher than 14 times the magnitude of the measured fan pressure rise. Compared to this range, the differences in the predicted static fan pressure rise for frozen rotor (**Figure 14**) and mixing plane (**Figure 15**) which is similar to the absolute value of the measured fan pressure rise are rather small.

The most significant difference between both contour plots is the pressure level on the radial outside of the pole gap. Locally restrained to this circumferential position, the pressure is visibly higher for frozen rotor than for mixing plane.

The reason for this is that for the mixing plane interface, circumferential averaging of pressure and velocity leads to a well-distributed flow in the stator core ventilation ducts. Compared to this, for the frozen rotor interface, an increased amount of airflow is directly guided into the ventilation ducts at the same

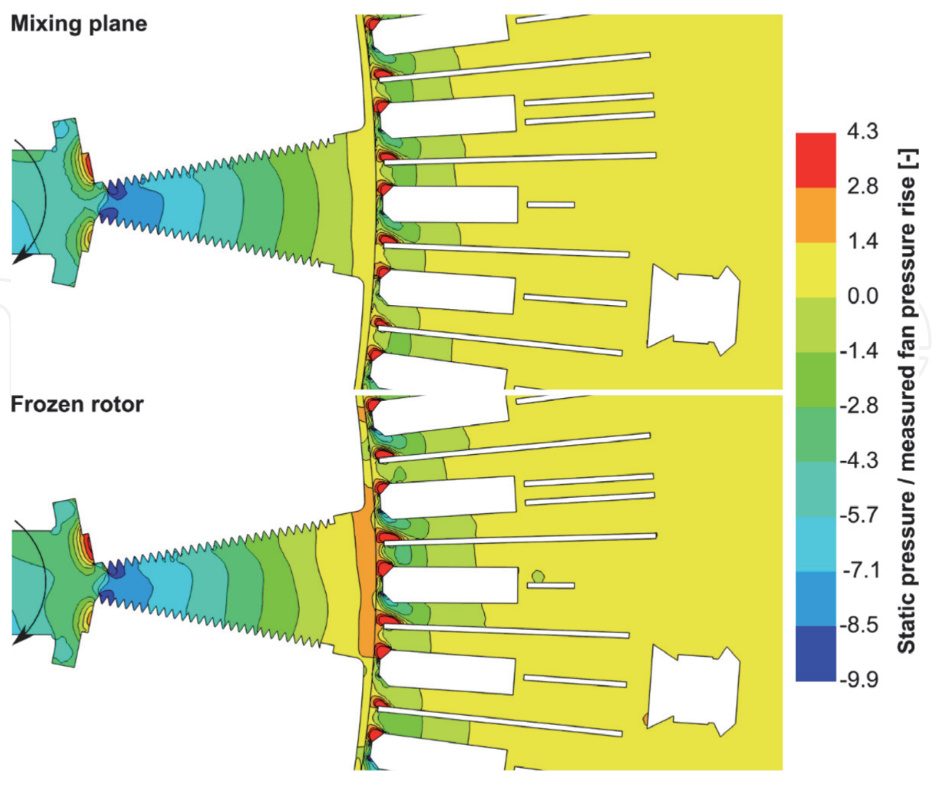

Figure 16.
Static pressure contour plot through the axial center of machine. Rotor pole gap, air gap, and stator core ventilation ducts are visible. Operating point is 750 rpm machine speed and fans turned off. Mixing plane (top) and frozen rotor (bottom) interface. Values normalized by the magnitude of the measured fan pressure rise at the investigated operating point.

circumferential position as the pole gap. Therefore, with the total mass flow being determined by the model boundary conditions, the pressure loss locally increases in the stator ducts in this position. In contrast to this effect, the circumferentially even flow distribution for the mixing plane interface leads to a comparably smaller overall pressure drop over the stator core ventilation ducts.

The described local increase of pressure radially outside of the pole gap for the frozen rotor interface propagates in upstream direction through the pole gap and eventually leads to the previously described differences in the performance maps of **Figures 14** and **15**.

5.3 Dimensionless machine parameters

It is a common practice to design hydro generator ventilation systems using analytical evaluations based on dimensionless parameters. Thus, in this section the capability to predict such dimensionless parameters shall be investigated for the CFD models. An approach to describe the pressure loss of a generator by three coefficients that can be assumed to be constant for geometrically similar machines is presented in [8]. In this method, a pressure loss coefficient ζ that is assumed to be proportional with the flowrate to the power of two is calculated for the machine in standstill. This yields the formula

$$\Delta p_{M,stat}(n, \dot{V}) = \Delta p_M(n = 0, \dot{V}) = \rho\zeta\frac{\dot{V}^2}{{D_I}^4}, \tag{4}$$

where D_I is the inner diameter of the stator, n the rotational speed of the electric machine, and $\dot{V}$ the volumetric flowrate of the cooling circuit. The equation above shows a quadratic dependency with $\dot{V}$, whereas ζ is the only unknown. Therefore, the coefficient ζ can be derived from fitting this quadratic function to the measured and calculated machine pressure loss data in generator standstill. This was done using the least squares method for measurement and CFD.

For the rotating machine, another two coefficients that contribute to the pressure balance are defined in [8]. The coefficient ε represents an additional pressure loss due to machine rotation and is assumed to be proportional with the flowrate and the rotational speed; the coefficient ψ_0 represents the pressure buildup due to the rotating runner and is assumed to be proportional with the rotational speed to the power of two. Therefore, the pressure contribution by the rotating machine can be described as

$$\Delta p_{M,rot}(n, \dot{V}) = \rho\left[\varepsilon\frac{\dot{V}n}{D_I} + \psi_0 n^2 {D_I}^2\right]. \tag{5}$$

The most convenient way to derive the coefficients ε and ψ_0 from the measured data is to introduce two dimensionless parameters. The first parameter is the pressure number

$$\psi = \frac{\Delta p}{\rho n^2 {D_I}^2} \tag{6}$$

and the second parameter is the volume number

$$\varphi = \frac{\dot{V}}{n{D_I}^3}. \tag{7}$$

Inserting Eqs. (6) and (7) in (5) yields the dimensionless formula:

$$\psi_{M,rot}(\varphi) = \varepsilon\varphi + \psi_0. \tag{8}$$

Note that this equation is only valid for the rotating machine but becomes undefined for the generator in standstill. The advantage of the dimensionless form is that it only depends on one variable which is the volume number φ. By fitting the linear right hand side of Eq. (8) to the measured and calculated data using a least squares approach, the coefficients ε and ψ_0 can be derived.

The total machine pressure loss is the sum of the stationary and the rotating pressure loss. With Eqs. (4), (7), and (8), the machine pressure number can be described as

$$\psi_M(\varphi) = \psi_{M,stat}(\varphi) + \psi_{M,rot}(\varphi) = \zeta\varphi^2 + \varepsilon\varphi + \psi_0. \tag{9}$$

For the given machine, the influences of ζ and ψ_0 are dominating the pressure loss, whereas ε only has a small influence within the investigated operating range.

Figure 17 shows the pressure number ψ_M over the volume number φ for the measurement and the CFD simulations with frozen rotor and mixing plane interface. At lower volume numbers, both simulations underestimate the pressure number, whereas both simulations tend to overestimate the pressure number for higher volume numbers.

The mixing plane interface approximates the measurement results better for higher volume numbers and the frozen rotor interface for lower volume numbers. The evaluated operating points, excluding those without machine rotation, which are used to derive the necessary parameters described above, are also shown in **Figure 17** exemplarily for the simulation with mixing plane interface. These points help to understand the deviation between the two investigated interfaces. Most of the points for the highest machine rotation rate (blue crosses) correspond to lower volume numbers in comparison to the points for the mid rotation rate (gray crosses). Therefore, for this generator, the low-volume numbers are mainly

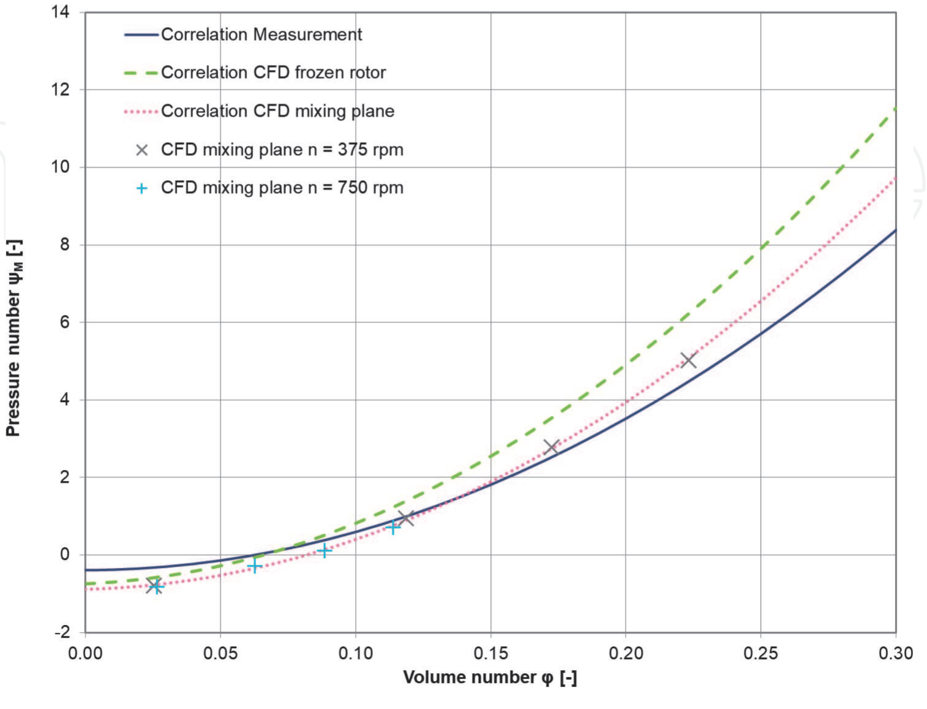

Figure 17.
Dimensionless machine pressure loss.

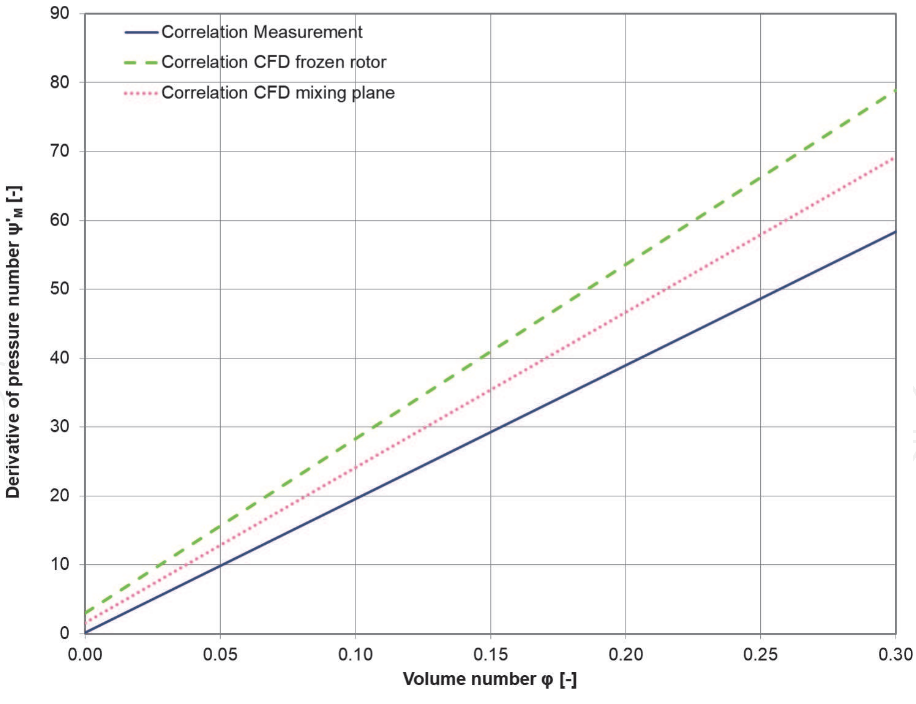

Figure 18.
Derivative of the dimensionless machine pressure loss.

influenced by the operating points with high rotational machine speeds. Comparable to Section 5.2, the frozen rotor interface leads to better results for the highest machine rotation speed, and therefore, the deviation between measurement and CFD simulation with frozen rotor interface is lower for low-volume numbers. For high-volume numbers, the influence of the medium machine speeds is higher, and therefore, the mixing plane interface results are closer to the measurement.

Figure 18 shows the derivative of the pressure number with respect to the volume number and therefore the gradients of the curves in **Figure 17**. The curves in **Figure 18** mainly show the influence of the pressure loss coefficient ζ (Eq. (9)). The lowest gradient can be observed for the measurements followed by the mixing plane interface and the frozen rotor interface. Therefore, the mixing plane interface approximates the gradient of the pressure number in dependency of the volume number to be more accurate in comparison to the frozen rotor interface, for the given machine configuration.

6. Summary and conclusions

Due to the need of detailed measurement data to validate simulation tools, Voith Hydro designed and built a model generator which allows the investigation of new generator design features or different configurations, e.g., different ventilation concepts. In this chapter, one specific ventilation concept was described.

Measurements and CFD simulations were conducted and compared to each other. The measurements showed the expected machine behavior and are therefore perfectly suitable to validate the presented simulation approaches. All in all, four simulation configurations were investigated which consist of two different rotor-stator interfaces and two turbulence models.

A comparison of the pressure paths showed that the combination of mixing plane interface and k-ε turbulence model overestimates the pressure drop between winding overhang and hot air compartment, whereas all other configurations showed a good prediction of the whole pressure path. The best approximation of the pressure path was reached with the mixing plane interface and the k-ω SST turbulence model, for the presented operating point.

For all other investigations, only the k-ω SST turbulence model was considered.

Looking at the fan performance map, good overall agreement between CFD and measurement was found for both investigated rotor-stator interfaces. However, there are several operating ranges where one of the interfaces is superior to the other one. A comparison of the dimensionless machine pressure loss showed that the curve gradients were resolved better with the mixing plane interface.

All in all it can be concluded that both combinations of rotor-stator interfaces and the k-ω SST turbulence model match the measurement data of the given ventilation concept well. This justifies the application of the presented simulation approach in the design of hydro power generator ventilation and cooling systems. Qualitatively, all measured flow effects were reproduced in the CFD simulations. When predicting absolute pressure levels, some deviations between measurement and CFD were present especially at lower flowrates, but in general good agreement was found over the full operating range.

As future work it is recommended to further investigate the effect of the chosen rotor-stator interface on the simulation accuracy for different operating conditions. In this context, transient simulations might be conducted for selected operating points. On the test rig, different ventilation concepts will be realized and investigated similarly to the measurement approach presented in this chapter. Furthermore, the model generator additionally is equipped with numerous temperature measurement sensors, providing validation data for even more detailed conjugate heat transfer simulations, which will also be investigated in future work.

Author details

Bastian Diebel, Axel Walter-Krause*, Roland Jester-Zuerker and Babette Schwarz
Voith Hydro Holding GmbH & Co. KG, Heidenheim, Germany

*Address all correspondence to: axel.walter-krause@voith.com

References

[1] ISO 5801:2017-09. Fans-Performance Testing Using Standardized Airways. Geneva, Switzerland: International Organization for Standardization; 2017

[2] Munson BR, Young DF, Okiishi TH. Fundamentals of Fluid Mechanics. J. Wiley & Sons: Hoboken, NJ; 2006

[3] Vogt B, Lahres S. Calculation of cooling and ventilation of large hydro generators with advanced 3D numerical simulations. In: Proceedings of the International HYDRO Conference; Austria. 2013

[4] Ferziger J, Peric M. Computational Methods for Fluid Dynamics. Berlin, Heidelberg: Springer; 2012

[5] Shih TH, Liou WW, Shabbir A, Yang Z, Zhu J. A new k-ε eddy viscosity model for high Reynolds number turbulent flows. Computers & Fluids. 1995;**24**(3):227-238

[6] Menter FR. Two-equation eddy-viscosity turbulence models for engineering applications. AIAA Journal. 1994;**32**(8):1598-1605

[7] Menter FR, Kuntz M, Langtry R. Ten years of industrial experience with the SST turbulence model. In: Hanjalić K, Nagano Y, Tummers MJ, editors. Turbulence, Heat and Mass Transfer 4. New York, NY: Begell House, Inc.; 2003. pp. 625-632

[8] Liebe W. Ueber das aerodynamische Verhalten elektrischer Maschinen. Siemens Zeitschrift. Berlin; 1957